Click Here for Full Article

Martian atmosphere as observed by VIRTIS-M on Rosetta spacecraft

A. Coradini,[1] D. Grassi,[1] F. Capaccioni,[2] G. Filacchione,[2] F. Tosi,[1] E. Ammannito,[1]
M. C. De Sanctis,[2] V. Formisano,[1] P. Wolkenberg,[1] G. Rinaldi,[1] G. Arnold,[3]
M. A. Barucci,[4] G. Bellucci,[1] J. Benkhoff,[5] J. P. Bibring,[6] A. Blanco,[7]
D. Bockelee-Morvan,[4] M. T. Capria,[2] R. Carlson,[8] U. Carsenty,[3] P. Cerroni,[2]
L. Colangeli,[9] M. Combes,[4] M. Combi,[10] J. Crovisier,[4] P. Drossart,[4] T. Encrenaz,[4]
S. Erard,[4] C. Federico,[11] U. Fink,[12] S. Fonti,[7] W.-H. Ip,[13] P. G. J. Irwin,[14] R. Jaumann,[3]
E. Kuehrt,[3] Y. Langevin,[6] G. Magni,[2] T. McCord,[15] V. Mennella,[9] S. Mottola,[3]
G. Neukum,[3] V. Orofino,[7] P. Palumbo,[16] G. Piccioni,[2] H. Rauer,[3] B. Schmitt,[17]
D. Tiphene,[4] F. W. Taylor,[14] and G. P. Tozzi[18]

[1] The Rosetta spacecraft accomplished a flyby of Mars on its way to 67P/Churyumov-Gerasimenko on 25 February 2007. In this paper we describe the measurements obtained by the M channel of the Visual and Infrared Thermal Imaging Spectrometer (VIRTIS-M) and the first scientific results derived from their analysis. The broad spectral coverage of the VIRTIS-M in the IR permitted the study of various phenomena occurring in the Martian atmosphere; observations were further exploited to achieve accurate absolute radiometric calibration. Nighttime data from the VIRTIS-M constrain the air temperature profile in the lower atmosphere (5–30 km), using variations in CO_2 opacity at 4.3 μm. A comparison of this data with the global circulation model (GCM) by Forget et al. (1999) shows a trend of slightly higher air temperature in the VIRTIS-M retrievals; this is accompanied by the presence of moderate decreases (~5 K) in large sections of the equatorial region. This is potentially related to the occurrence of water ice clouds. Daytime data from the VIRTIS-M reveal CO_2 non–local thermodynamic equilibrium emission in the high atmosphere. A mapping of emission intensity confirms its strict dependence on solar zenith angle. Additionally, devoted limb observations allowed the retrieval of vertical emission intensity profiles, indicating a peak around 105 km in southern tropical regions. Ozone content can be effectively monitored by the emission of O_2 ($a^1\Delta_g$) at 1.27 μm. Retrieved emission intensity shows that polar regions are particularly rich in ozone. Aerosol scattering was observed in the 1–2.5 μm region above the night region above the night disk, suggesting the occurrence of very high noctilucent clouds.

Citation: Coradini, A., et al. (2010), Martian atmosphere as observed by VIRTIS-M on Rosetta spacecraft, *J. Geophys. Res.*, *115*, E04004, doi:10.1029/2009JE003345.

[1]INAF, IFSI, Rome, Italy.
[2]INAF, IASF, Rome, Italy.
[3]DLR, Berlin, Germany.
[4]Observatoire de Paris, Meudon, France.
[5]European Space Research and Technology Centre, European Space Agency, Noordwijk, Netherlands.
[6]IAS, Centre universitaire d'Orsay, Orsay, France.
[7]Dipartimento di Fisica, Università del Salento, Lecce, Italy.
[8]Jet Propulsion Laboratory, NASA, Pasadena, California, USA.
[9]Osservatorio Astronomico di Capodimonte, INAF, Naples, Italy.
[10]Atmospheric, Oceanic, and Space Sciences, University of Michigan, Ann Arbor, Michigan, USA.
[11]Dipartimento di Scienze della Terra, Università di Perugia, Perugia, Italy.

[12]Department of Planetary Sciences, Lunar and Planetary Laboratory, Tucson, Arizona, USA.
[13]Graduate Institute of Astronomy, National Central University, Chung-Li, Taiwan.
[14]Atmospheric, Oceanic and Planetary Physics, University of Oxford, Oxford, UK.
[15]Bear Fight Center, Winthrop, Washington, USA.
[16]Dipartimento di Scienze Applicate, Università degli Studi di Napoli "Parthenope," Naples, Italy.
[17]OSUG, Université Joseph Fourier, Grenoble, France.
[18]Osservatorio Astrofisico di Arcetri, INAF, Firenze, Italy.

1. Introduction

[2] Flyby observations of targets of opportunity have successfully contributed to the study of many important phenomena in our solar system. Relevant examples include

Table 1. Position of the VIRTIS-M Order Filters[a]

Filter Name	Affected Region (nm)
VIS: $218 < b < 224$	640–651
IR 1: $45 < b < 62$	1415–1576
IR 2: $148 < b < 165$	2388–2548
IR 3: $284 < b < 294$	3671–3765
IR 4: $349 < b < 359$	4284–4379

[a]The band index (i.e., the index of spectrum sampling point), counted from the low-wavelength side, is indicated by b.

observations of Venus and Jupiter by Galileo and Cassini spacecraft, respectively [e.g., *Carlson et al.*, 1991; *Porco et al.*, 2003]. These events additionally provide an opportunity to check spacecraft and instrument status, validate operational concepts, perform calibrations, and deliver preliminary science return. This last aspect often offers a unique chance to make observations of the target of opportunity, using instrumentation with better performance characteristics than those of spacecraft dedicated to the target. In addition, these flybys may yield unusual and opportunistic observational geometries.

[3] The Rosetta spacecraft of the European Space Agency performed a flyby of Mars on 25 February 2007. The Rosetta mission is devoted to the study of a comet and its environment (originally 46P/ Wirtanen, now 67P/Churyumov-Gerasimenko). Even though the payload components were designed and highly optimized for that purpose [*Schulz et al.*, 2004], the flexible design of instruments allowed the acquisition of synoptical observations over wide areas of the planet. Despite the numerous missions dedicated to the study of the Martian environment, the daily evolution of the atmosphere has not been extensively studied by satellites. All orbiters were actually placed in polar orbits to maximize surface coverage, resulting either in data sets collected at fixed local time (in the case of Sun synchronous orbits, such as Mars Global Surveyor) or in strong local time-latitude-season correlations (e.g., Mars Express).

[4] In this paper we focus our attention on the observations made using the M channel of the Visual and Infrared Thermal Imaging Spectrometer (VIRTIS-M). In section 2, we provide a description of the instrument and its radiometric performances. The Mars flyby represented a fundamental validation test for our calibration pipeline, and the methods are described extensively. In section 3, the Martian VIRTIS-M data set is discussed, providing the scientific rationale for observations and examples of spectra. In section 4, we illustrate the main science themes that can be addressed on the basis of our data. Covered topics include thermal structure of the lower atmosphere, non–local thermodynamic equilibrium (non-LTE) emission, aerosol content, and ozone emission. This discussion is not all-inclusive, and additional studies are proposed in the conclusions.

2. Instrument Description and Performances

[5] The VIRTIS instrument consists of two main channels that provide a double capability: (1) high-spatial-resolution (up to an instantaneous field of view, or IFOV, of 250 μrad) visible and IR imaging in the 0.25–5.2 μm range at moderate spectral resolution (VIRTIS-M channel) and (2) high spectral resolution spectroscopy in the 2–5.2 μm range (VIRTIS-H channel). The two channels observe in tandem the same areas in combined modes to take full advantage of their complementarity.

[6] The VIRTIS-M is characterized by a single optical head consisting of a Shafer telescope combined with an Offner imaging spectrometer and by two bidimensional focal plane assemblies (FPAs): the visible light spectrometer (VIS) (0.25–1.1 μm) and IR (1–5.2 μm). The VIRTIS-M is actually an imaging spectrometer, able to acquire a stack of monochromatic images ("cubes") that allow the spectrum to be reconstructed for each pixel.

[7] The VIRTIS-M operates simultaneously in the visible and IR domains, with spectral sampling steps of 1.88 and 9.43 nm respectively. The VIRTIS-M, like most hyperspectral imagers, is a slit spectrometer: the optical system perfectly matches a Shafer telescope to an Offner grating spectrometer to disperse a line image across two bidimensional focal planes. A silicon CCD is used to perform hyperspectral imaging from 0.25 to 1 μm, while a mercury cadmium telluride (HgCdTe) IR focal plane array takes care of the 1–5.2 μm spectral range. A scan mirror is used to achieve full imaging capability. Overlapped on the two VIRTIS-M detectors are filters needed to remove higher diffraction orders (order filters). The filters edges fall at fixed positions along the VIRTIS-M spectra, creating regions where calibration is more problematic and that have therefore been neglected in the present analysis. Table 1 reports the filters positions for the VIRTIS-M.

[8] The VIRTIS-H is a high-resolution IR cross-dispersed spectrometer using a prism and a grating. The 2–5.2 μm spectrum is dispersed in 10 orders on a focal plane detector array. The VIRTIS-M and VIRTIS-H IFOVs are 0.25 × 0.25 mrad (for an individual pixel) and 1.74 × 0.58 mrad.

[9] The hearts of the instrument are the FPAs (Table 2). The CCD in the VIRTIS-M is a frame transfer device. The CCD specifications are listed in Table 2. The baseline for both the VIRTIS-M and VIRTIS-H IRFPAs are HgCdTe on sapphire substrates. To reduce dark current, the VIRTIS-M IRFPA must be cooled to below 70 K. Passive cooling has been rejected because the low emissive power of passive radiators and the risk of comet contamination indicate a minimum radiator area larger than 1 m^2. Cryocoolers are suitable for the VIRTIS FPA cooling task.

2.1. Calibration

[10] A detailed description of the instrument and its calibration on ground has been given in several papers [*Coradini et al.*, 1999, 2004; *Coradini and the VIRTIS team*, 2007; *Ammannito et al.*, 2006; *Filacchione et al.*, 2006], and here we report only a very short summary.

[11] The performances of the instrument were tested both in laboratory and in flight. Before the integration of the VIRTIS experiment aboard Rosetta, several tests were performed on the VIRTIS-M and VIRTIS-H channels to completely characterize the instrumental performances.

[12] The fundamental calibrations necessary to correctly retrieve the scientific information from VIRTIS data are as follows: (1) Geometric calibration is the measurement of IFOV, FOV, and in-field distortions. (2) Spectral calibration is the correlation between the spectral dispersion axis of the

Table 2. Characteristics and Performances of the VIRTIS Focal Planes

	VIRTIS-M CCD	VIRTIS-M IRFPA	VIRTIS-H IRFPA
Material	Silicon + UV coating	HgCdTe on AlO$_2$ or CdZnTe	HgCdTe on AlO$_2$ or CdZnTe
Pixel pitch (μm)	38	38	38
Format	256 × 432	256 × 432	240 × 640
Noise (rms e$^-$)	<20	280	280
Full well capacity (e$^-$)	10^6	1.6×10^7	7×10^6
Temperature (K)	155	75 or 90	70 or 85
Dark current (e/s)	<1	72,000	18,000

focal planes and the wavelength. (3) Spatial calibration is the evaluation of the flat field matrices necessary to uniform the focal planes responses. (4) Radiometric calibration is the determination of the instrument transfer function, which allows the conversion of digital numbers in physical units of spectral radiance (W m^{-2} μm^{-1} sterad^{-1}). These quantities, continuously checked during the flight at each switch on of the experiment, are used in the data pipeline before the scientific analysis.

[13] *Ammannito et al.* [2006] describe the spectral and geometric calibrations, while the paper of *Filacchione et al.* [2006] concerns the measurements of flat fields and radiometric and internal calibrations. A more detailed analysis of the methods used to characterize imaging spectrometers by using on-ground and flight data can be found in the work of *Filacchione* [2006], where a description of the calibration pipelines of both the Cassini Visual and Infrared Mapping Spectrometer-V (VIMS-V) and Rosetta VIRTIS-M experiments is given.

2.2. Radiometric Calibration Refinement

[14] The close encounter with Mars represented an important opportunity to improve the VIRTIS-M calibration defined in laboratory preflight tests, as reported in the Rosetta book [*Coradini et al.*, 2009].

[15] The Martian data set acquired during the flyby is used to perform a smooth calibration in the visible range by using the Hubble Space Telescope (HST) spectra [*Noe Dobrea et al.*, 2003, 2008] in the VIS range and Mars Express–Omega data in the IR range (ibid).

[16] The in-flight radiometric calibration is computed in correspondence of a 60 × 60 km plain region near the Gusev Crater. We assign to these two raw spectra the corresponding calibrated reflectance, measured with similar observation and seasonal conditions by the HST/Near Infrared Camera and Multi-Object Spectrometer in the visible range and by Mars Express-Omega in the IR: furthermore, these data are interpolated at VIRTIS-M spectral resolutions.

[17] In this way, we recalibrate the VIRTIS data in the spectral range 1.0–2.0 μm. The obtained calibration holds for the center of the VIRTIS-M slit. To extend the calibration to the rest of the slit, we use the flat field of the experiment obtained in the laboratory. The flat field data take into account the differences in the response of the VIRTIS in different zones of the slit and at different wavelengths. In this way, the VIRTIS-M as a whole could be radiometrically calibrated. We instead use the results of the ground-based calibration data in the 2.0–5.0 μm range. This "hybrid method" has been also used to calibrate other imaging spectrometers, such as the VIMS [*Brown et al.*, 2004].

2.3. Geometry Information

[18] The VIRTIS-M radiometric data are integrated using geometric information from the SPICE ancillary data system [*Acton*, 1996] and the time of acquisition. For each pixel covering the planet's disk, the geographic coordinates of the pixel's centroid as well as the emission, incidence, and phase angles were computed. The minimum altitude of the line of sight above the planet's areoid was computed for pixels covering the limb. Because of a flight software bug, certain spectral cubes were subject to a loss of the acquisition times for some frame lines. This resulted in missing geometry information for the respective pixel lines.

3. VIRTIS Martian Data Set

[19] This work considers only data from the VIRTIS-M IR subsystem, which we will refer to as VIRTIS from here on. The term "channel" will be used to indicate an individual spectral sampling point.

[20] The VIRTIS observations took place between 24 February 2007 18.14 UTC and 25 February 7.33 UTC. In Martian terminology, these values correspond to Martian year 28 and solar longitude 189, written as MY28 and $L_S = 189$. The gravity assist geometry and derived thermal, power, and communication conditions strongly constrained the observation possibilities during the Mars flyby; for example, science operations were not allowed during the closest approach. Throughout the flyby, the subspacecraft point remained within [30S, 90E] and [30N, 150E]. This constrained most observation opportunities to the Eastern Hemisphere of the planet. The observations can be placed into three categories:

[21] 1. Preflyby observations yielded a total of 13 spectral cubes. The approach geometry enabled hyperspectral imaging of the entire visible side of the Martian disk in daytime conditions. Observation time totaled 4 h at a phase angle of 15°, which remained relatively constant. Range from the center of the planet to the spacecraft varied from 1.2×10^5 to 2.5×10^5 km, correlating to a ground resolution between 30 and 60 km.

[22] 2. Postflyby observations yielded 2 cubes for 8 limb scans. These observations focused on atmospheric emissions at the limb. A maximum vertical resolution of 15 km was obtained, corresponding to a range of 4×10^4 km at a phase angle of 155°.

[23] 3. Later postflyby observations yielded 4 cubes and were focused on thermal emissions in the 3–5.2 μm range. Analysis of these data allows monitoring of temperature conditions in the lower atmosphere. The larger range dis-
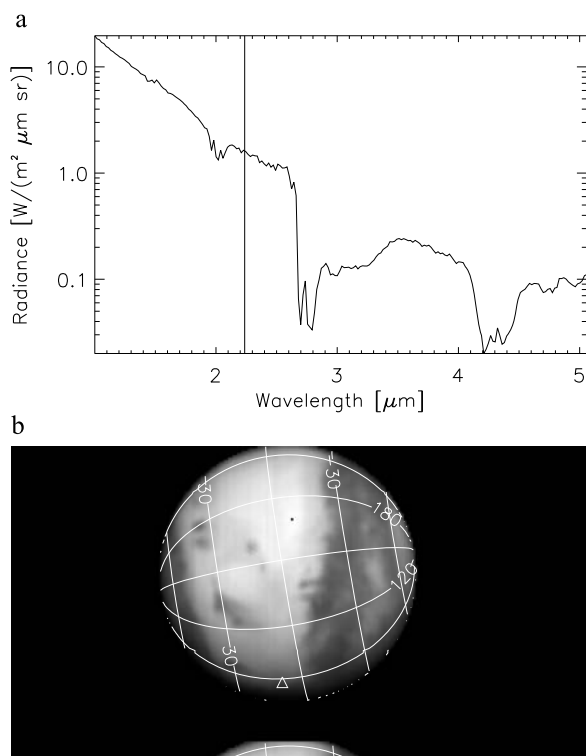
Figure 1. (a) Typical VIRTIS Martian daytime spectrum. (b) VIRTIS frame at 2.24 μm, from cube I1_00130962500. Exposure time was 0.2 s. The triangle marks the position where the spectrum of Figure 1a was extracted.

tance enabled imaging of the entire disk of the planet, almost completely in darkness.

[24] Table 3 summarizes the characteristics of different observations. Typical frames and spectra for the three different observational categories are presented in Figures 1–3. Different radiance levels observed by VITRIS during the three phases previously discussed required the application of different exposure times (detailed in the captions of Figures 1–3).

[25] Daytime measurements in the range 1–3.5 μm are dominated by the surface reflectance of incoming solar radiation (Figure 1a); this reflectance is driven by the mineralogy and physical conditions of the soil. In this spectral range, absorption bands of the main atmosphere component CO_2 are evident at 2.8, 2, 1.6, and 1.42 μm. The 2.8 μm band is saturated, while the other three bands show much weaker intensities and can be used to study the pressure at surface level across the disk by mapping their depths [Spiga et al., 2007].

[26] Around 3.5 μm, thermal emission of surface and atmosphere becomes important. The thermal range is characterized by a very intense CO_2 band at 4.3 μm. In theory, the shape of this band is driven by the air temperature profile in the conditions of LTE. However, the VIRTIS data of the daytime Martian atmosphere present the strong emissions in the bottom of the 4.3 μm band expected by Lòpez-Valverde et al. [2005] as a result of non-LTE emissions.

[27] Aerosols were also observed by the VIRTIS. Martian dust is expected to be quite featureless in the spectral range

covered by the VIRTIS [Ockert-Bell et al., 1997] and is therefore difficult to monitor. However, Martian climatology recorded by the Thermal Emission Spectrometer (TES) [Smith, 2004] forecasts a low dust content around L_s = 190 in absence of great dust storms; fortunately, the excellent visibility of surface albedo features in the VIRTIS frames excluded the occurrence of these storms. On the contrary, water ice (including surface frost and suspended clouds) is characterized by typical bands at 3 and 1.5 μm; this fact was used to create a water ice map from the VIRTIS cube.

[28] Spectral features of minor gases are also seen in VIRTIS data. In several spectra, it is possible to detect O_2 ($a^1\Delta_g$) emission at 1.27 μm. This species is usually adopted as a proxy for ozone [Fedorova et al., 2006]. The main CO band can be observed between 4.73 and 4.82 μm. A water vapor line is seen at 2.62 μm. Unfortunately, the strongest absorption features of this band fall within the order filter.

[29] In nighttime data, only the thermal component of the spectrum is observed (Figure 2a). In this case, LTE assumptions are valid. Consequently, the 4.3 μm CO_2 band has been modeled to compute the thermal profile in the lower atmosphere, adapting the methods presented by Grassi et al. [2008].
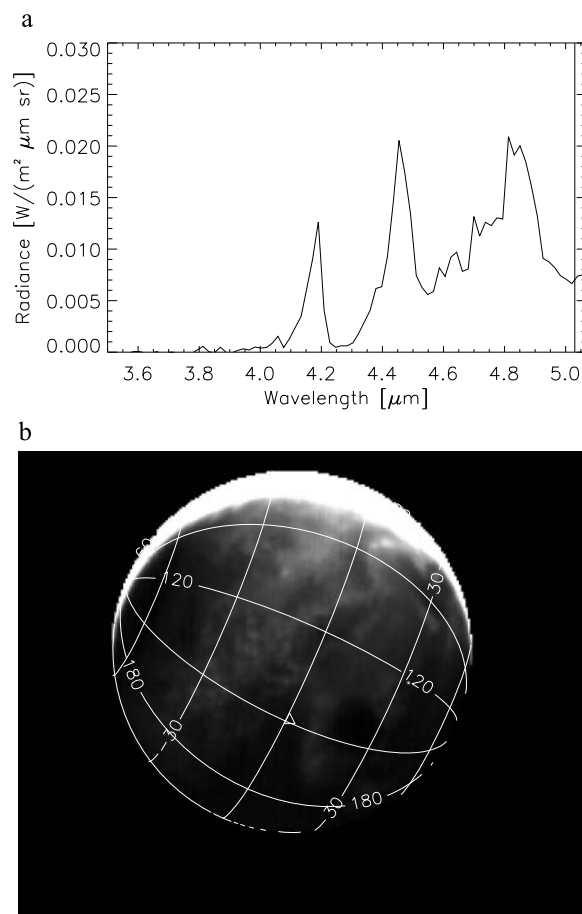

Figure 2. (a) Typical VIRTIS Martian nighttime spectrum. (b) VIRTIS frame at 5.05 μm, from cube I1_00131007789. Exposure time was 1 s. The triangle marks the position where the spectrum of Figure 1a was extracted.

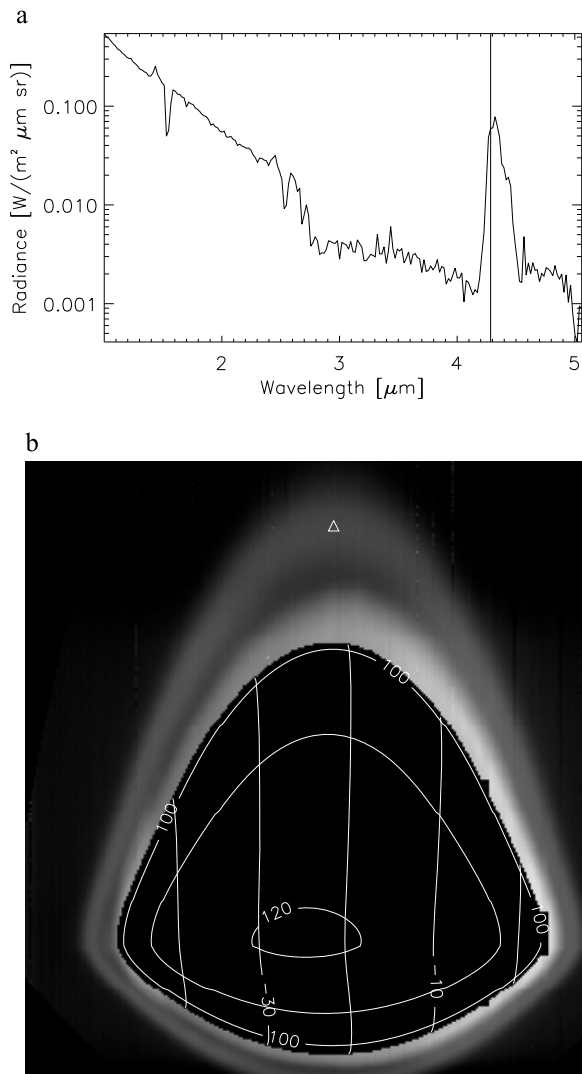**Figure 3.** (a) VIRTIS Martian limb spectrum, acquired above the morning terminator. (b) VIRTIS frame at 4.28 μm, from cube I1_00130995150. Exposure time was 0.7 s. The triangle marks the position where the spectrum of Figure 3a was extracted.

[30] Limb measurements from the VIRTIS (Figure 3a) can be extremely complex to interpret. This is in part due to long optical paths, which may make indistinguishable the various different physical conditions along the line of sight. Moreover, the absence of radiation from a background surface enhances the relative importance of scattering. In our data set, the tangential points, where most of the atmospheric mass lying along the path is found, are in full sunlight. As a result, effects from non-LTE CO_2, from ozone emission, and from scattering of sunlight are observed and remain extremely complex to model. In monochromatic images (Figure 3b), the disk appears deformed because of a combination of the rapid spacecraft motion during closest approach and the method for acquiring limb scans, which consisted of taking two consecutive scans in opposite directions covering the same portion of the disk.

[31] The VIRTIS data most closely resemble that of OMEGA [*Bibring*, 2007], a spectro-imager operating on Mars Express in the same spectral range. While OMEGA data are superior in spatial and seasonal coverage and spatial resolution, the VIRTIS provides an ideal complement because of its higher spectral resolution in the mapping channel, the specific observing conditions during flyby that allowed synoptic measurements on wide regions of the planet, and superior performances in the thermal region.

4. Data Analysis

[32] This section describes the current status of scientific analysis of the VIRTIS observations. Priority was given to studies that could take advantage of the synoptical nature of the data and that could be assessed on a quantitative basis using software tools currently available to the team.

4.1. Nighttime Air Temperature Maps

[33] The retrieval of air temperature profiles in the lower Martian atmosphere, on the basis of CO_2 opacity in the thermal IR, has been performed on regular basis from the data of several instruments: IRIS-Mariner 9 [*Conrath*, 1975], TES-Mars Global Surveyor [*Conrath et al.*, 2000], and Planetary Fourier Spectrometer (PFS) Mars Express [*Grassi et al.*, 2005]. The algorithms presented in these papers rely on variation of CO_2 opacity with wavelength inside the observed bands. If the spectral resolution of observation is adequate, different sampling points in the spectrum measure the radiance thermally emitted at different levels (namely, where the opacity reaches a value about one), allowing, by inversion, the reconstruction of vertical air temperature profile.

[34] The experiments mentioned above have been operated in the mid-IR and measure the 15 μm CO_2 band, but this band lies well outside the spectral range covered by our instrument. On the other hand, the 4.3 μm CO_2 band has been successfully adopted in the air temperature retrieval in Venus mesosphere from the VIRTIS–Venus Express data by *Grassi et al.* [2008]. The code used in this study has been adapted to Martian conditions and has been applied to the VIRTIS–Rosetta data.

[35] Figure 4 shows the shapes of weighting functions for selected channels. Information content of data is higher for the indicative levels of 0.2 and 2 mb (around 30 and 10 km above the surface), where, on the basis of the Venus Express numerical experiments [*Grassi et al.*, 2008], an error less than 2 K can be expected. The vertical resolution of retrieved profile is comparable to weighting functions width, i.e., 10 km.

[36] The retrieval procedure consisted of two consecutive steps:

[37] 1. In the first step, the code modeled the continuum outside the band, driven mostly by surface temperature T_{surf} and emission $\varepsilon(\lambda)$. The latter parameter is an unknown function of wavelength and we cannot achieve, in strict terms, a unique solution, since we had as data the radiance measured in N channels and as unknowns the N values of ε at the same sampling channels and T_{surf}. We therefore *assumed* a constant value of ε and computed the best-fit values for T_{surf} and ε by means of a least squares algorithm.

Table 3. Summary of VIRTIS-M IR Observations at Mars[a]

Cube Name	Frame Size (pixels)	Observation Phase	Data Type
I1_00130961622	256 × 122	Preflyby	Dayside, entire disk
I1_00130962500	256 × 148	Preflyby	Dayside, entire disk
I1_00130963310	256 × 149	Preflyby	Dayside, entire disk
I1_00130964121	256 × 149	Preflyby	Dayside, entire disk
I1_00130964930	256 × 148	Preflyby	Dayside, entire disk
I1_00130965741	256 × 161	Preflyby	Dayside, entire disk
I1_00130966610	256 × 161	Preflyby	Dayside, entire disk
I1_00130967541	256 × 185	Preflyby	Dayside, entire disk
I1_00130972041	256 × 89	Preflyby	Dayside, portion of disk for mosaicking
I1_00130972701	256 × 88	Preflyby	Dayside, portion of disk for mosaicking
I1_00130973361	256 × 89	Preflyby	Dayside, portion of disk for mosaicking
I1_00130974021	256 × 89	Preflyby	Dayside, portion of disk for mosaicking
I1_00130974741	256 × 246	Preflyby	Dayside, entire disk (highest spatial resolution)
I1_00130995150	256 × 288	Postflyby	Limb above morning terminator (two scans at highest spatial resolution)
I1_00130999629	256 × 869	Postflyby	Limb above morning terminator (six scans at lower resolution)
I1_00131004789	256 × 119	Postflyby	Nightside, portion of disk
I1_00131006589	256 × 119	Postflyby	Nightside, portion of disk
I1_00131007789	256 × 221	Postflyby	Nightside, entire disk
I1_00131009589	256 × 221	Postflyby	Nightside, entire disk

[a]Each pixel in a frame has a corresponding spectrum of 432 sampling points (e.g., I1_00130999629 provides 256 × 869 = 2,22,464 spectra). The cubes are ordered according acquisition time.

[38] 2. Once the level of the continuum was defined, the shape of the CO_2 band was modeled varying the temperature profile.

[39] Following the Venusian case [*Grassi et al.*, 2008], we adopted for step 2 a nonlinear relaxation algorithm, initialized with an isothermal profile. This approach avoided any bias from the a priori profile required by the Bayesian formalism [*Rodgers*, 2000], which is more appropriate when dealing with data with higher information content. Surface pressure was taken from the *pres0* subroutine included in the European Martian Climate Database (EMCD) V4.2 (http://www-mars.lmd.jussieu.fr/ [*Lewis et al.*, 1999]). The iteration was stopped by fulfillment of a χ^2 test on radiance or after a maximum of six iterations, to avoid the growth of spurious high-spatial-frequency components.

[40] Figure 5 compares, for some typical cases, the radiance measured by the VIRTIS and the simulation derived from the retrieval code result. Major misfits are observed in the range 4.55–4.75 μm, where CO, seen by the VIRTIS but not modeled by our code, has its fundamental band.

[41] Retrievals can be performed, on individual pixel basis, for nighttime measurements (the non-LTE emission precludes the method applicability during daytime conditions). In order to increase the S/N and to reduce computational times, the VIRTIS pixels were binned, channel by channel, on 2 × 2 widths. Code outputs were filtered to reject cases where lack of convergence or high emission angle (greater that 60°) was found. Resulting maps for the 2 mb level are presented in Figure 6. The maps are obtained by using the geometrical information associated with the VIRTIS cubes and are shown in cylindrical projection. These data are the first extensive synoptic map of temperatures of the Martian lower atmosphere recorded so far.
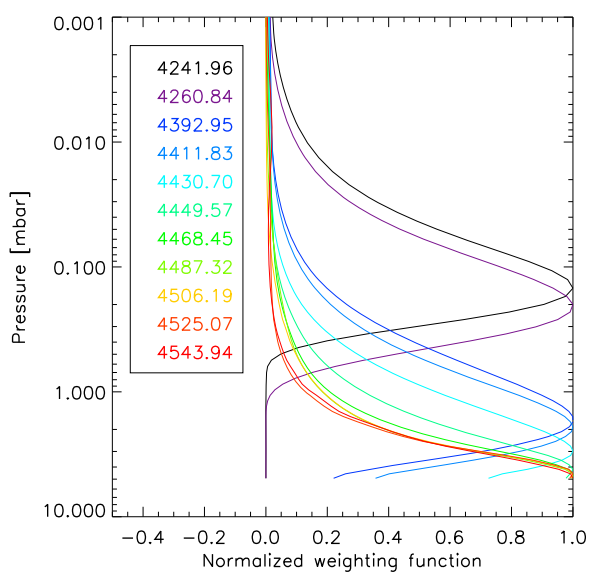
Figure 4. Normalized weighting functions for the VIRTIS channels in the region of 4.3 μm CO_2 band.
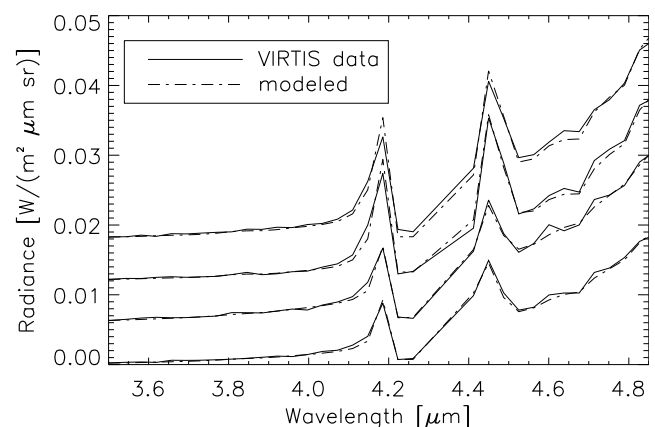
Figure 5. Examples of retrieval code capability to model the radiances measured by VIRTIS. Major misfits are observed in the range 4.55–4.75 μm, where CO, not modeled by our code, has its fundamental band.
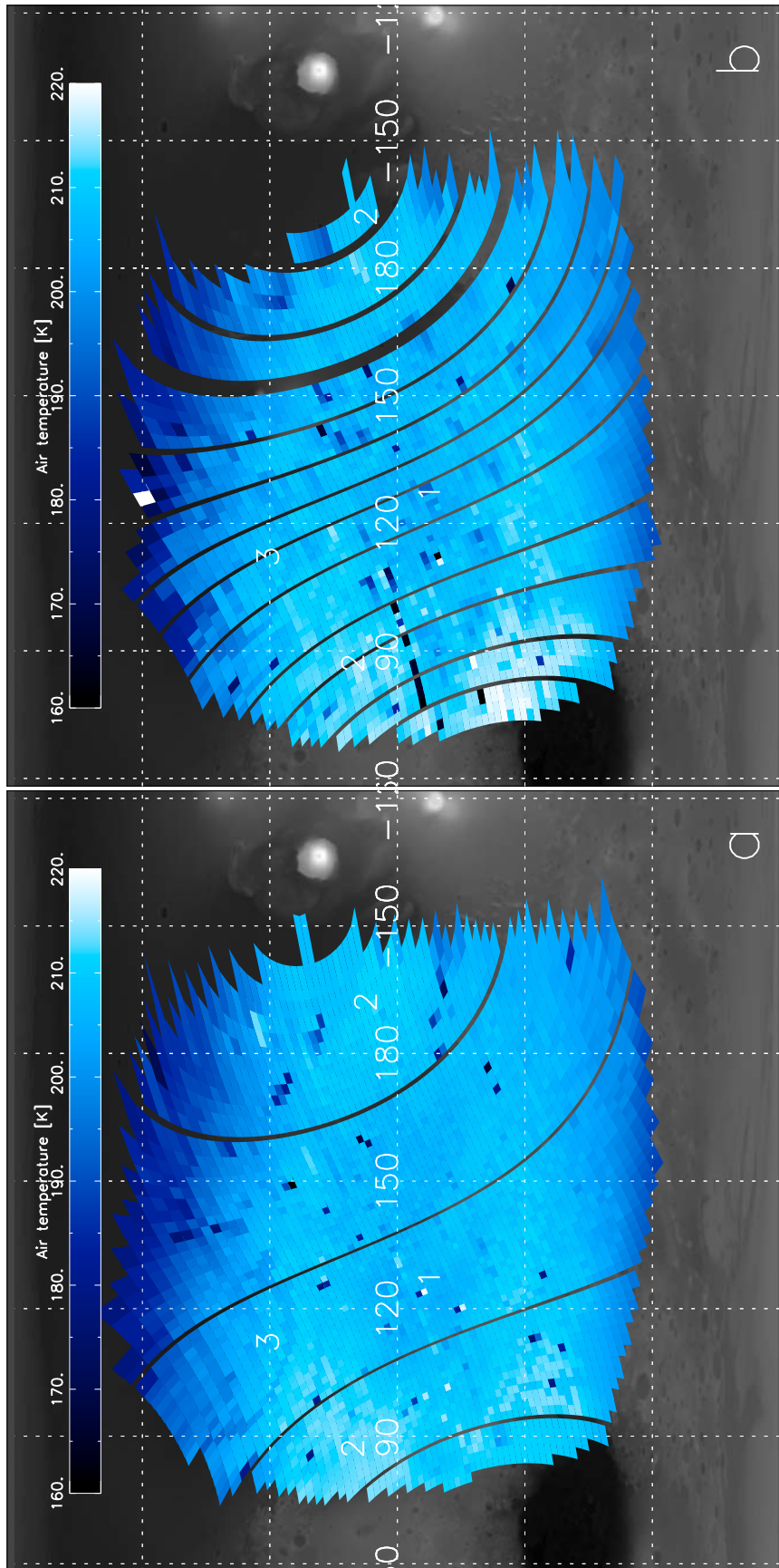
Figure 6. (a) Air temperatures at the 2 mbar level, as retrieved from cube I1_00131007789. The black stripes are due to missing geometry data. Data are projected in cylindrical coordinates. Among other features, we mention the following: the extended minimum of temperature along the equator, between 100°E and 170°E (marked as 1); the two local maxima at 90°E and 190°E (marked as 2); the extended cold air "arch" that runs from 100°E, 30°N to 130°E, 30°N, reaching a minimum latitude of 25°N at 110°E (marked as 3). (b) The same for cube I1_00131009589. The lower quality of results is likely to be ascribed to the lossy compression algorithm applied to this cube prior to Earth downlink.

[42] Air temperature fields exhibit a detailed structure. The regions at higher latitudes appear colder, as expected. A small-magnitude, but spatially extended, minimum of temperature is observed along the equator, between 100°E and 170°E. At 0° latitude, temperature has two local maxima at 90°E and 190°E. An extended cold air "arch" runs from 100°E, 30°N to 130°E, 30°N, reaching a minimum latitude of 25°N at 110°E. Apparently, this arch is not related to any topographic feature. Temperature maps from two distinct VIRTIS cubes acquired 30 min apart both present the details described above, despite the movement of planet disk with respect to the instrument focal plane, confirming that they are genuine features of the Martian atmosphere. Retrievals from cube I1_00131009589 better cover the eastern rims of Hellas, where a local maximum is observed.

[43] The maps at the 0.2 mbar level present a much noisier appearance, since this region is constrained by a much smaller number of the VIRTIS sampling channels. Nevertheless, we can appreciate in this pressure range a monotonous temperature decrease from west (dusk side) toward east (dawn side).

[44] Values of air temperature were compared against the expectations of EMCD 4.2. The latter are derived from the results of the GCM described by *Forget et al.* [1999]. Differential maps (VIRTIS-EMCD) are given in Figure 7. It is noteworthy that despite a retrieval approach totally independent from model expectations, we achieve a very close quantitative correspondence. Differences never exceed 8 K at the 2 mbar level and tend to be moderately positive between 15°N and 45°N and around 30°S. Conversely, the equatorial region presents usually a temperature deficiency, which reaches a value of 5 K around 150°E in the data from both the VIRTIS cubes.

[45] The VIRTIS observations are performed in a season usually characterized by a low water ice and dust opacity [*Smith*, 2004]. However, the TES climatology is derived mostly from early afternoon observations (14 local time) and cannot account for the likely daily basis variations of the ice content [*Formisano et al.*, 2001, *Smith et al.*, 2006] driven by temperature changes. Consequently, the occurrence of substantial ice load during nighttime cannot be excluded. The presence of water ice has a twofold effect on our retrievals:

[46] 1. Water ice in the atmosphere may represent an additional source of opacity and may induce a depression of radiance level. If this opacity is not consistently taken into account during retrieval, resulting temperatures may be underestimated.

[47] 2. Water ice is an effective IR emitter because of its strong band at 12 μm and its radiative effects, currently not included in the EMCD-parent GCM, may induce cooling in the order of few kelvins at the pressure levels considered here [*Wilson et al.*, 2008].

[48] The first effect induces therefore a systematic error in our retrievals, while the second is a genuine air temperature variation. Even if the limited spectral nighttime coverage of the VIRTIS data does not allow a self-consistent simultaneous retrieval of the water ice content (and therefore the disentangling between the two effects mentioned above), we still consider water ice as the most likely cause of the observed temperature deficiency. In particular, the ice content map discussed in section 4.4 points toward a substantial increase of ice load during the night as well as to a local ice enhancement at 30°S in the very early morning, both facts being consistent with our interpretation of temperature maps (area of temperature deficiency shifts from equator to 30°S in the eastern part of area observed in Figure 7a). Preliminary analysis of the VIRTIS-M visible data also suggests the occurrence of water ice clouds at the morning terminator. It is noteworthy that these pieces of evidence are derived from large-scale spatial analysis of ice load and its correlation with air temperatures is made possible only by the unique characteristics of the VIRTIS Martian data set.

4.2. Non-LTE Emissions

[49] Non-LTE emission from the region of 4.3 μm band was first reported in the Infrared Space Observatory data by *Lellouch et al.* [2000] and was later described in the PFS data by *Lòpez-Valverde et al.* [2005] and *Formisano et al.* [2006]. Despite the theoretical capability to provide a numerical modeling of this phenomenon, its inclusion in a complete retrieval scheme has not yet been implemented, making it difficult to distinguish between this fluorescence, the thermal emission of atmosphere in the band wings, and scattering of solar radiation.

[50] In this section, we focus our attention on the VIRTIS channel centered at 4.28 μm. This sampling point lies well outside the VIRTIS order filter and in a spectral region where CO_2 is so intense that, according the numerical modeling of *Lòpez-Valverde et al.* [2005], the signal from an ideal pure LTE atmosphere would basically be zero. The effect of dust scattering is also attenuated in a deeply saturated spectral region, since most of the dust lies in the lower atmosphere, and solar photons cannot reach these altitudes. The absolute intensity of radiation observed at 4.28 μm is therefore a good proxy for true non-LTE emission efficiency.

[51] Figure 8a shows a map of non-LTE emission intensity on the Martian daytime hemisphere. A correction was introduced on the VIRTIS radiances to account for (1) increased emitting optical path (normalization for air mass) and (2) CO_2 residual absorption with increasing emission angle θ_{obs}. Pixels with $\theta_{obs} > 70°$ were neglected, since plane-parallel approximation adopted for evaluation of CO_2 residual absorption is not valid for high emission angles. In agreement with theoretical model expectations, the map highlights the very strong correlation of non-LTE emission with solar energy input (note that this correlation is also evident in not corrected data). Figure 9a provides a scatter plot of the VIRTIS corrected radiances versus the cosine of Sun incidence angle and a comparison against the expectations of *Lòpez-Valverde et al.* [2005]. Despite the higher spectral resolution, the latter represent just a lower boundary for values measured by the VIRTIS, suggesting either an actual underestimation of the efficiency of level-populating mechanisms in theoretical model or an additional contribution to non-LTE emission in driving the signal at 4.28 μm.

[52] Figure 8a furthermore indicates a local time dependence because, for the same values of Sun incidence angle, intensities on the western side (morning) appears systematically higher than their afternoon counterparts. Figure 9b illustrates this trend for two selected latitudes. Namely, at a given latitude, pixels observed during morning show higher signal than those observed in the afternoon at the
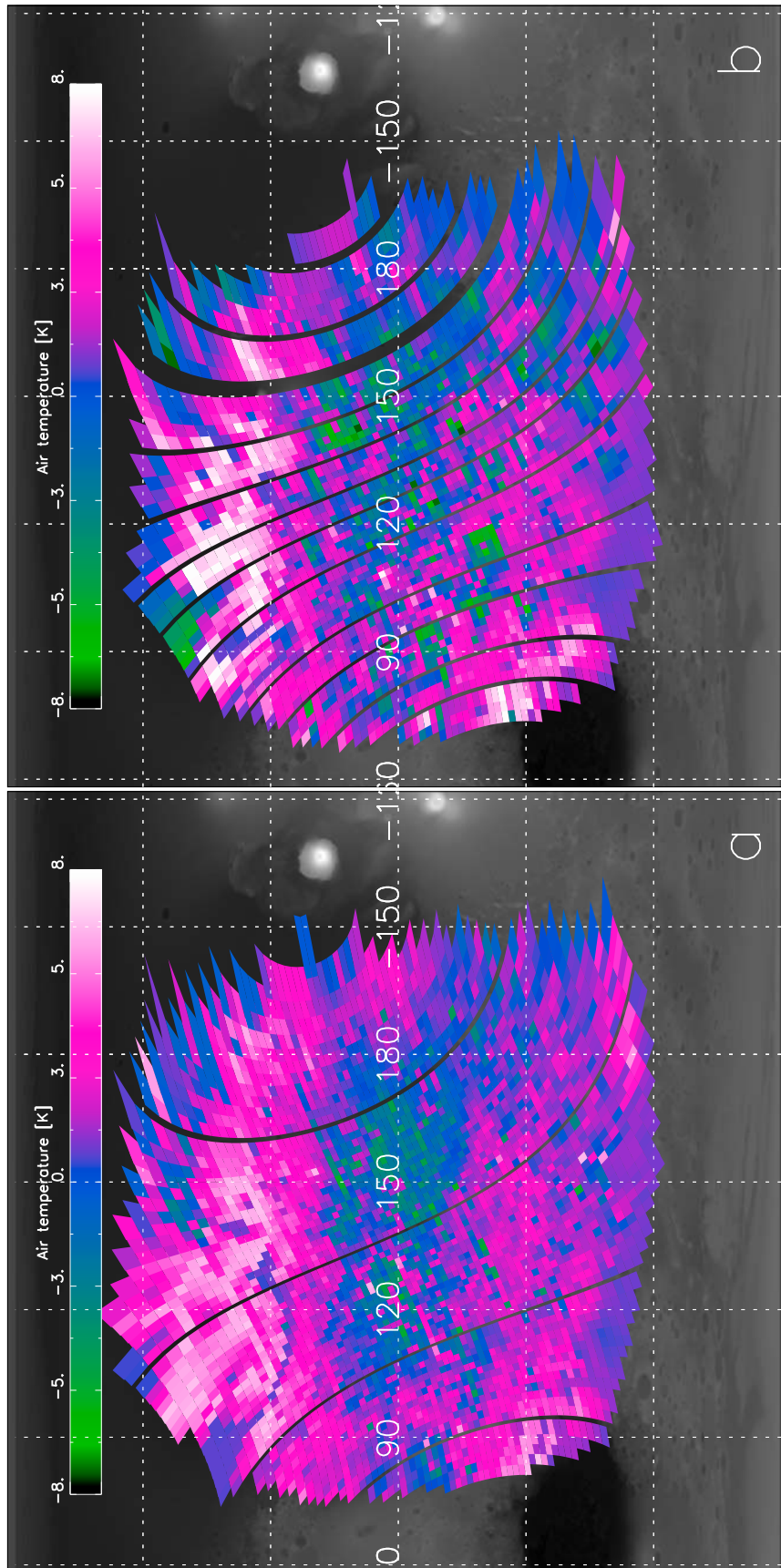
Figure 7. (a) Difference between Figure 6a and the EMCD expectations for air temperatures, for the same time and location. (b) The same as for Figure 6b.
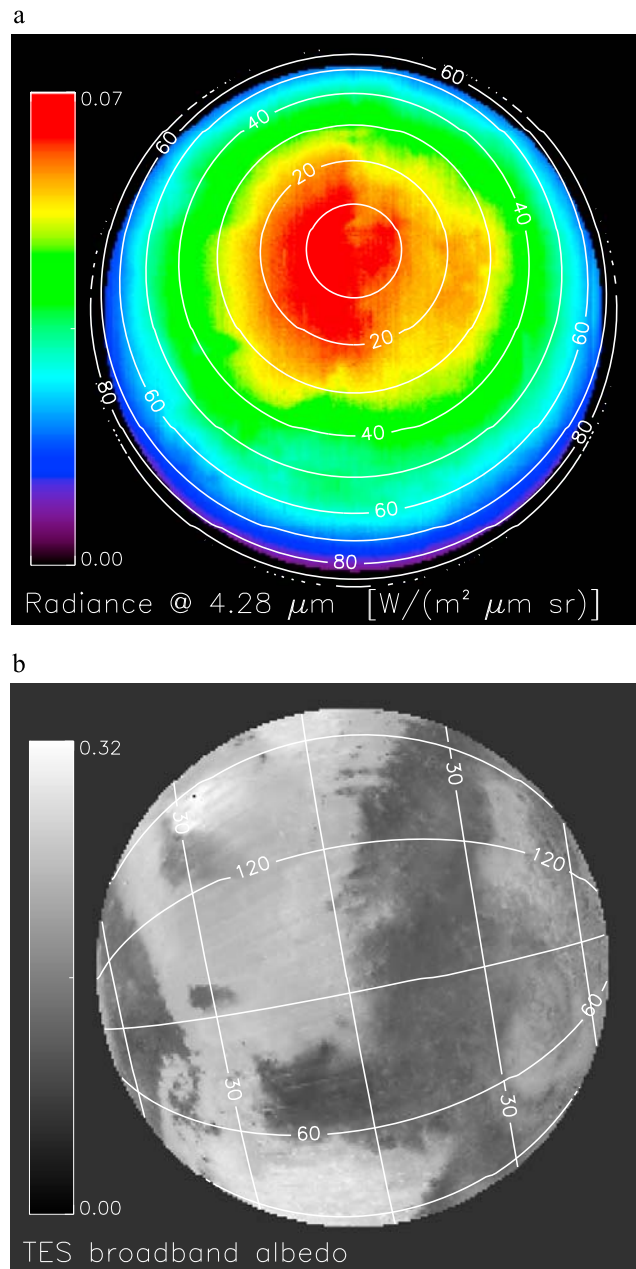
Figure 8. (a) Intensity of non-LTE emission at 4.28 μm derived from cube I1_00130974741. The level curves indicate the Sun zenith angle. (b) Broadband albedo of the observed portion of disk, as derived from TES maps [*Christensen et al.*, 2001].

same solar zenith angle. A peak efficiency around 11 LT is observed in both latitude ranges. This trend can be interpreted as due to an additional contribution to the signal measured at 4.28 μm by water ice scattering, since the water ice content tends to diminish when atmospheric temperature increases along the day (see section 4.4). Actually, direct numerical experiments demonstrated that signal measured at the bottom of the band (LTE components only) may increase by almost two orders of magnitude with respect to clear sky condition if an ice cloud of realistic opacity (0.26 at 3.1 μm) is

placed above the indicative altitude of 40 km. This value corresponds roughly to 10% of expected non-LTE emission and is quantitatively consistent with the morning/afternoon differences observed in Figure 9b.

[53] The vertical trend of non-LTE emission is another topic that could be addressed on the basis of the VIRTIS data, taking into account the postflyby limb observations. The solid curve in Figure 10a shows the intensity measured at 4.28 μm versus altitude, as derived from the cube in Figure 3b. The curve is an average of the radiances measured between columns 135 and 145, in the upper part of frame (i.e., in the area surrounding the diamond mark in Figure 3b). Scattering of solar radiation by aerosols and thermal emission of the atmosphere (background) account almost entirely for the signal measured between 0 and 50 km altitude. Actually, similar plots at nearby wavelengths not affected by CO_2 non-LTE emission show only this monotonically decreasing component. Conversely, at 4.28 μm we can appreciate a second peak, centered around 100 km, because of non-LTE emission. This result is in fair agreement with the trends reported in Figure 20 of the work of *Formisano et al.* [2006], once the different spectral and spatial resolutions of the VIRTIS and PFS are kept in mind. The non-LTE signal was deconvolved to account for spherical geometry view and residual CO_2 absorption, to allow separation from background and to retrieve the value of emission coefficient against altitude. Despite the nonuniqueness of solution for this inverse problem, results can be considered as robust above 90 km, where the emission is effectively modeled by a Gaussian function peaked at 115 km, with a standard deviation of 20 km and maximum intensity of $8.3 \times \cdot 10^{-10}$ W/(m^2 μm sr)/cm (Figure 10b).

4.3. O$_2$ ($a^1\Delta_g$)

[54] Mapping of O$_2$ ($a^1\Delta_g$) emission at 1.27 μm (Figure 11a) was performed according to the retrieval scheme detailed by *Fedorova et al.* [2006] for SPICAV observations. In this spectral range, VIRTIS has a spectral resolution lower than that of SPICAM, providing therefore a limited amount of sampling points suitable for emission and continuum definition. Eventually, this implied increased systematic errors. Further sources of errors with respect to SPICAV case are represented by (1) high Martian signal, which causes phenomena of saturation (for the adopted exposure time) in the central part of the disk, characterized by low Sun zenith angle and high surface albedo, and (2) residual flat field corrections. Combining these contributions, systematic retrieval errors up to 10 MR cannot be excluded. We decided therefore to apply, prior to emission retrieval, a high-pass filter with a threshold of 0.2 W/(m^2 μm sr) for the signal at 1.27 μm relative to local continuum in order to limit systematic effects on the final map. On the other hand, random errors due to individual pixel noise (more important for the definition of relative trends) remain below 5 MR. The final result is presented in Figure 11b. The main feature is the sharp emission enhancement above both polar regions, more evident on the Southern Hemisphere. Once the systematic errors are kept in mind, these figures are quantitatively consistent with the SPICAM results presented by *Fedorova et al.* [2006] (Figure 11b) and with the anticorrelation, first reported by *Krasnopolsky and Parshev*
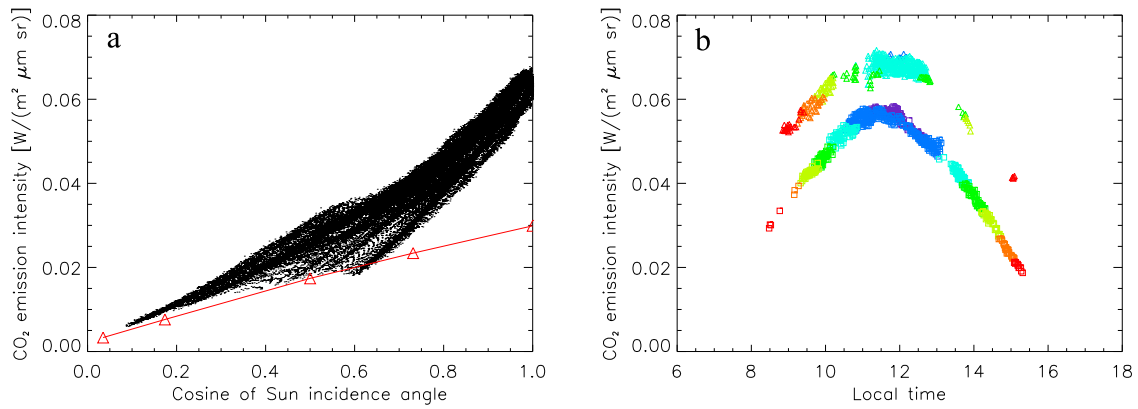
Figure 9. (a) Scatter plot of non-LTE emission intensity versus Sun zenith angle, as derived from the pixels in the 4.28 μm frame of cube I1_00130974741 (black points). the red triangles show the theoretical expectations from *Lòpez-Valverde et al.* [2005] (note that the estimates are for a higher spectral resolution and represent therefore an upper limit at VIRTIS resolution). (b) Scatter plot of non-LTE emission intensity versus local time, for two selected latitude bins. The color code of points gives their solar zenith angle. The lower point envelope is for latitude range [35°S, 30°S]; the upper envelope is for the altitude range [30°N, 35°N] and has an offset of 0.02 W/(m^2 μm sr).

[1979], of ozone and water vapor; the latter is expected to be highly depleted above polar caps in this Martian season [*Smith*, 2004].

[55] The VIRTIS data do not provide any evidence of emission on the night side of the planet's disk (Figure 12). This may allow us to pose an upper limit on the efficiency of O_2 ($a^1\Delta_g$) formation by three-body recombination [*Garcia*
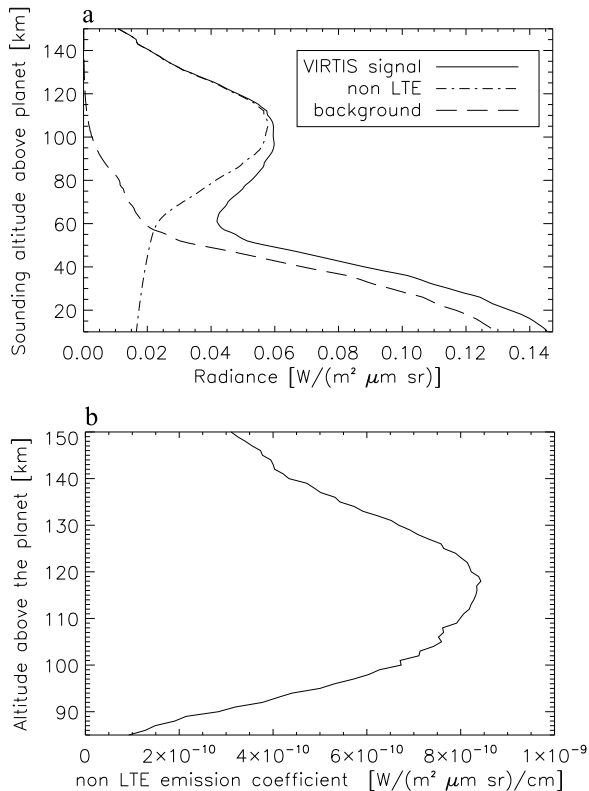

Figure 10. (a) VIRTIS observations of non-LTE emission at limb (4.28 μm). The solid curve denotes the observed radiance versus the altitude above the disk. The dashed line denotes the estimated contribution from aerosol background. The dashed-dotted line denotes the estimated contribution from non-LTE only. (b) Retrieved non-LTE emission coefficient versus altitude.
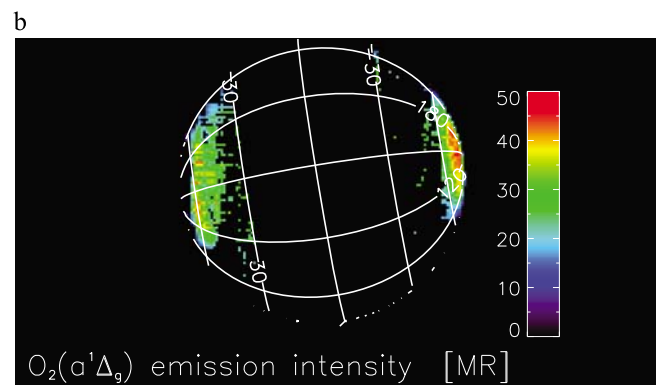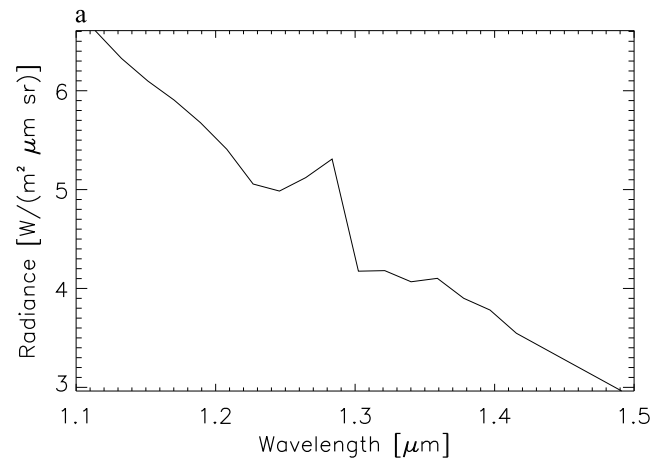
Figure 11. (a) Example of O_2 ($a^1\Delta_g$) emission at 1.27 μm as seen in the VIRTIS spectra. (b) Retrieved emission intensity of O_2 ($a^1\Delta_g$) at 1.27 μm, as derived from VIRTIS cube I1_00130962500 (dayside).
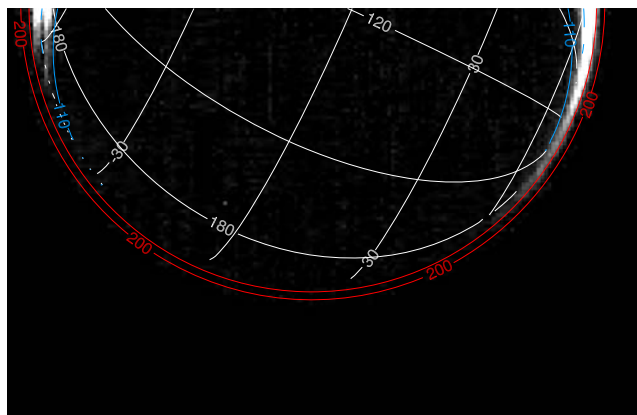
Figure 12. Relative intensity of O_2 ($a^1\Delta_g$) emission at 1.27 μm from VIRTIS cube PI72P732. The red level curves indicate 100 and 200 km of altitude above the disk edge. The blue level curves indicate the locus for 110° Sun zenith angle.

Munoz et al., 2005] of two oxygen atoms and a CO_2 molecule. The emission can be easily observed above the polar caps, where the planet limb remains in sunlight and ozone photodissociation can take place.

[56] Limb measurements (such as the ones presented in Figure 3b) allowed us to study the vertical profile of O_2 ($a^1\Delta_g$) for the early morning conditions (Figure 13). In our data, the Sun is already illuminating the limb of the planet, pointing toward ozone dissociation as the main source of emission. Unfortunately, during our observation sessions, the signal from the continuum (due to scattering of solar radiation by aerosols) was so high that the detector was saturated while observing at tangent altitudes lower than 65 km. Our results are therefore not directly comparable to the data derived by SPICAM stellar occultation described by *Lebonnois et al.* [2006]. Radiance profile is, within errors, monotonically decreasing from 65 to 100 km, where the signal reaches the effective noise level. Even if not deconvolved for limb view geometry, this excludes the occurrence of individual emission layers in this altitude range.

4.4. Aerosol

[57] Among the three main classes of Martian aerosols detected so far (H_2O and CO_2 ices, silicate dust), water ice clouds are the easiest to detect in the VIRTIS data, because of the typical bands centered around 3 and 1.5 μm. The depth of the former feature is by far more evident, but its usage in a retrieval scheme is made very difficult by the need to distinguish its effects from the hydration signature of surface materials. On the other hand, the 1.5 μm feature was successfully adopted in the analysis of the OMEGA data [*Gondet et al.*, 2006]. Our retrieval scheme is based on a parameterization of feature depth on the basis of (1) total ice load, (2) emission, and (3) Sun zenith angles. This parameterization was derived from a series of synthetic spectra computed for different input conditions, on the basis of the radiative transfer scheme described by *Ignatiev et al.* [2005]. This method further includes a multiple scattering treatment. The computations were performed assuming the size dis-

tribution "Type I" given by *Wolff and Clancy* [2003]. Ice loads are given in terms of total opacity at 830 cm^{-1}, to allow for a comparison against the TES values reported by *Smith* [2004]. Water ice cloud retrieval was not possible on polar areas, where surface ice features become dominant. On ice-free surfaces, band depth variations related to realistic albedo variation are within 10%. Other possible sources of systematic errors are represented by scattering approximations, assumption on particles properties (size distribution and refractive index), and residual flat field corrections. Effects of these sources are difficult to estimate, but systematic errors on retrieved opacity in the order of 0.2–0.3 cannot be excluded. Random error related to pixel-to-pixel noise variations is about 0.1–0.15.

[58] The final map of ice total content is given in Figure 14a. It is evident that the ice content depends on the solar energy input (i.e., local time). Morning (west) side of the image shows higher loads and deeper bands than its evening counterpart (Figure 15), suggesting that a substantial fraction of ice load outside polar regions is involved in the condensation and sublimation processes on a daily basis. Values observed toward the evening limb are probably overestimated because of the high viewing angle, but the increase of ice load with respect to disk center (midday) has to be considered as a genuine feature. In general terms, the ice daily cycle is more evident in our data than in the expectations of EMCD 4.2 (Figure 14b). It shall be noted that the "banded" structure of ice clouds included in the database is too thin to be clearly observed in our maps, since its opacity is comparable to retrieval errors. Conversely, the substantial local maximum along morning terminator located at 30°S is probably indicative of latitudinal variations of ice content on the night side of the planet. An evidence of clouds coverage on Elysium Mons (around 30°N, 150°E) is also found in our data, with an enhancement above surrounding areas stronger than expected from theoretical computations. Early afternoon ice loads outside polar regions are in quantitative agreement with the very low values reported by *Smith* [2004] for this season, where the aphelion cloud belt has almost completely disappeared (opacity <0.2).
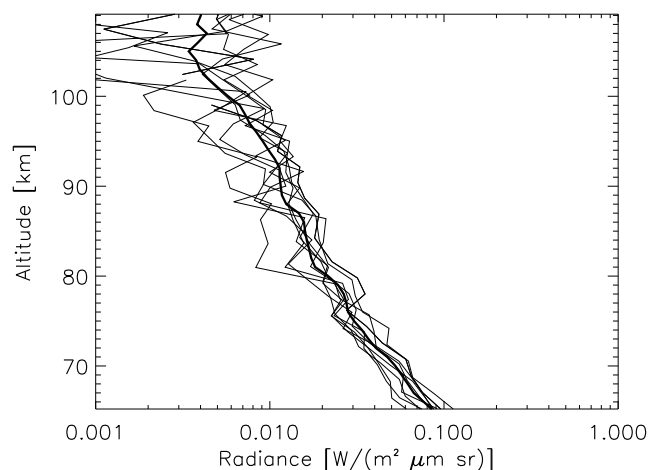

Figure 13. Intensity of O_2 ($a^1\Delta_g$) emission at 1.27 μm versus altitude, for eight columns extracted from cube I1_00130995150.

Figure 16. The observed radiance around 1.3 μm from VIRTIS cube I1_00131009589. The external curves indicate 100 and 200 km of altitude above the disk edge.
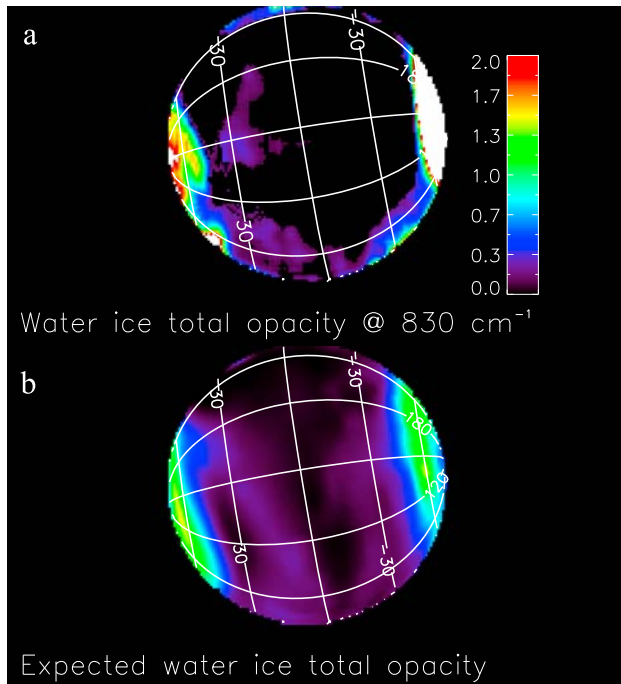
Figure 14. (a) Map of water ice load in the Martian atmosphere, as derived from VIRTIS cube I1_00130962500. (b) Water ice load in the Martian atmosphere expected by EMCD 4.2 (for cold atmosphere scenario), at the time and location of VIRTIS observation of Figure 14a.

[59] The VIRTIS limb data provide possible evidence of aerosol occurrence at very high altitudes, by measurements above the night limb (Figure 16). In this case, in the latitude range 20°N–40°S, we can appreciate sunlight scattered from the opposite side of the planet. Despite the low spatial resolution of this image, the radial radiance profile does not appear monotonously decreasing with altitude, with the strongest deviation from monotonicity at 15°S. This fact and the longitudinal confinement of radiance suggest that aerosols, instead of gases, are the responsible scattering
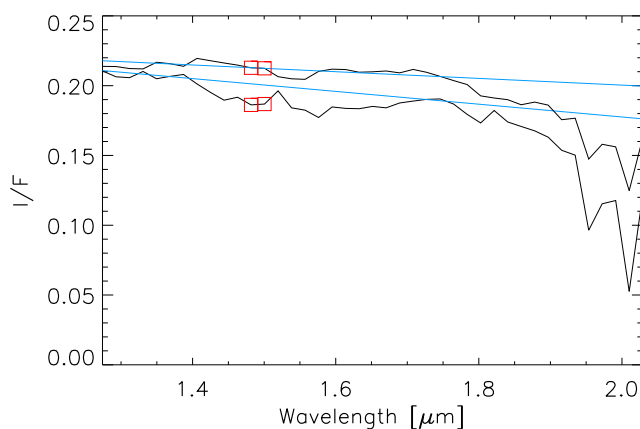

Figure 15. Comparison of two spectra acquired at the morning (lower curve) and evening (upper curve) sides of Mars disk. Note the difference in the depth of 1.5 μm water ice band depth with respect to local continuum (in blue).
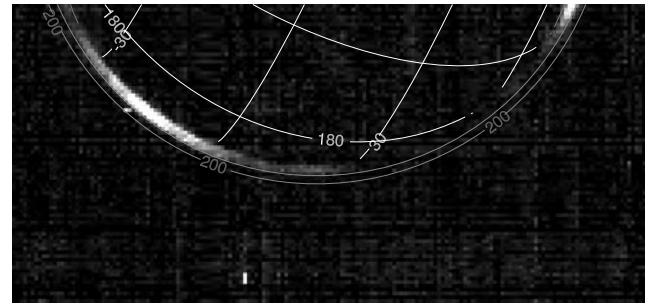
centers. In this case, a minimum altitude of 100 km for clouds top can be inferred from this image.

[60] The occurrence of high clouds on Mars has been reported for this latitude range by *Montmessin et al.* [2006], in forms of detached layers. These authors interpreted the SPICAM data as evidence of subtropical CO_2 clouds during the Martian night. Daytime nadir measurements by OMEGA [*Montmessin et al.*, 2007] further confirmed this interpretation. The spectral shape of clouds observed by the VIRTIS (Figure 17) presents no firm evidence of the 4.3 μm peak diagnostic of CO_2 ice according [*Montmessin et al.*, 2007]. These authors however considered nadir-looking measurement, and at the current date, we cannot exclude that this spectral feature may eventually become much fainter in our limb measurement.

5. Conclusions

[61] The VIRTIS made a series of successful observations during the Martian flyby, providing preliminary validation of the calibration to be used in later phases of the mission. Moreover, it demonstrated the flexibility of the instrument that was operated according very complex modes not foreseen in the original design (e.g., the double scan limb observation of Figure 3b).

[62] The VIRTIS observations acquired multispectral images on large areas of the planet, allowing the gathering of data simultaneously on a wide range of local times. This synoptic nature of data allowed us to achieve the following goals: (1) to identify the correlation between air temperature minima and water ice content, (2) to study local time trends of water ice, (3) to map the daily variations of non-LTE CO_2 emission, and (4) to highlight the occurrence of latitudinal-confined high-altitude clouds. These findings provide incentive for planning similar observations using other spacecrafts.

[63] Most of the analysis presented here relied on approximate algorithms, leaving room for substantial future improvements. In addition, the VIRTIS data will be essential in addressing several other investigations, mostly by comparison with the existing simultaneous observations by Mars Express instruments during Rosetta flyby. Among them, we mention the large-scale mapping of surface pressure and total CO content and the study of possible correlations between regional air temperature maps and topographic features.
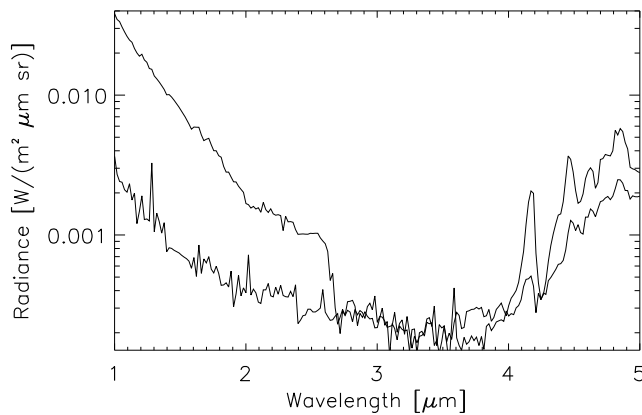
Figure 17. Average spectra from two selected regions of Figure 16. Both curves refer to the pixel above planet disk, with the altitude below 200 km. The upper curve is for 20°S–10°S; the lower curve is for 50°N–70°N.

References

Acton, C. H. (1996), Ancillary data services of NASA's navigation and ancillary information facility, *Planet. Space Sci.*, *44*, 65–70, doi:10.1016/0032-0633(95)00107-7.

Ammannito, E., G. Filacchione, A. Coradini, F. Capaccioni, G. Piccioni, M. C. De Sanctis, M. Dami, and A. Barbis (2006), On ground characterization of Rosetta/VIRTIS-M. I. Spectral and geometrical calibrations, *Rev. Sci. Instrum.*, *77*, 093109, doi:10.1063/1.2349308.

Bibring, J.-P. (2007), Introduction to special section: OMEGA/Mars Express Mars surface and atmospheric properties, *J. Geophys. Res.*, *112*, E08S01, doi:10.1029/2007JE002935.

Brown, R. H., et al. (2004), The Cassini Visual and Infrared Mapping Spectrometer (VIMS) investigation, *Space Sci. Rev.*, *115*, 111–168, doi:10.1007/s11214-004-1453-x.

Carlson, R. W., K. H. Baines, L. W. Kamp, P. R. Weissman, W. D. Smythe, A. C. Ocampo, T. V. Johnson, D. L. Matson, J. B. Pollack, and D. Grinspoon (1991), Galileo infrared imaging spectroscopy measurements at Venus, *Science*, *253*, 1541–1548, doi:10.1126/science.253.5027.1541.

Christensen, P. R., et al. (2001), Mars Global Surveyor Thermal Emission Spectrometer experiment: Investigation description and surface science results, *J. Geophys. Res.*, *106*(10), 23,823–23,872, doi:10.1029/2000JE001370.

Conrath, B. J. (1975), Thermal structure of the Martian atmosphere during the dissipation of the dust storm of 1971, *Icarus*, *24*, 36–46, doi:10.1016/0019-1035(75)90156-6.

Conrath, B. J., J. C. Pearl, M. D. Smith, W. C. Maguire, P. R. Christensen, S. Dason, and M. S. Kaelberer (2000), Mars Global Surveyor Thermal Emission Spectrometer (TES) observations: Atmospheric temperatures during aerobraking and science phasing, *J. Geophys. Res.*, *105*(4), 9509–9520, doi:10.1029/1999JE001095.

Coradini, A. and VIRTIS team (2007), VIRTIS: An imaging spectrometer for the Rosetta mission, *Space Sci. Rev.*, *128*, 529–559, doi:10.1007/s11214-006-9127-5.

Coradini, A., F. Capaccioni, P. Drossart, A. Semery, G. Arnold, and U. Schade (1999), VIRTIS: The imaging spectrometer of the Rosetta mission, *Adv. Space Res.*, *24*, 1105, doi:10.1016/S0273-1177(99)00691-2.

Coradini, A., F. Capaccioni, G. Filacchione, G. Magni, E. Ammannito, M. T. Capria, G. Piccioni, P. Drossart, and G. Arnold (2004), VIRTIS experiment at Churyumov-Gerasimenko comet, new Rosetta target, in *The New ROSETTA Targets*, edited by L. Colangeli et al., pp. 223–236, Kluwer Acad., Dordrecht, Netherlands.

Coradini, A., et al. (2009), VIRTIS: An imaging spectrometer for the Rosetta mission, in *Rosetta: ESA's Mission to the Origin of the Solar System*, edited by R. Schulz et al., Springer, New York.

Fedorova, A., O. Korablev, S. Perrier, J.-L. Bertaux, F. Lefevre, and A. Rodin (2006), Observation of O2 1.27 μm dayglow by SPICAM IR: Seasonal distribution for the first Martian year of Mars Express, *J. Geophys. Res.*, *111*, E09S07, doi:10.1029/2006JE002694.

Filacchione, G. (2006), Calibrazioni a terra e prestazioni in volo di spettrometri ad immagine nel visibile e nel vicino infrarosso per l'esplorazione planetaria, Ph.D. diss., Univ. degli studi di Napoli Federico II, Naples, (Available at ftp.iasf-roma.inaf.it/gianrico/phd/Filacchione_PHD_2006.pdf).

Filacchione, G., E. Ammannito, A. Coradini, F. Capaccioni, G. Piccioni, M. C. De Sanctis, M. Dami, and A. Barbis (2006), On ground characterization of Rosetta/VIRTIS-M. Part II: Spatial and radiometric calibrations, *Rev. Sci. Instrum.*, *77*, 103106, doi:10.1063/1.2360786.

Forget, F., F. Hourdin, R. Fournier, C. Hourdin, O. Talagrand, M. Collins, S. R. Lewis, P. L. Read, and J.-P. Huot (1999), Improved general circulation models of the Martian atmosphere from the surface to above 80 km, *J. Geophys. Res.*, *104*(E10), 24,155–24,176, doi:10.1029/1999JE001025.

Formisano, V., D. Grassi, N. I. Ignatiev, and L. Zasova (2001), IRIS Mariner 9 data revisited: Water and dust daily cycles, *Planet. Space Sci.*, *49*, 1331–1346, doi:10.1016/S0032-0633(01)00044-7.

Formisano, V., A. Maturilli, M. Giuranna, E. D'Aversa, and M. A. Lopez-Valverde (2006), Observations of non-LTE emission at 4,5 microns with the planetary Fourier spectrometer aboard the Mars Express mission, *Icarus*, *182*, 51–67, doi:10.1016/j.icarus.2005.12.022.

Garcia Munoz, A., J. C. McConnell, I. C. McDane, and S. M. L. Melo (2005), Airglow on Mars: Some model expectations for the OH Meinel bands and the O2 IR atmospheric band, *Icarus*, *176*, 75–95, doi:10.1016/j.icarus.2005.01.006.

Gondet, B., J.-P. Bibring, Y. Langevin, F. Poulet, F. Montmessin, and F. Forget (2006), One Martian year observation of H2O ice clouds by OMEGA/Mars Express, paper presented at the Second Workshop on Mars Atmosphere Modelling and Observations, Cent. Natl. D'Etudes Spatiales, 27 Feb. to 3 Mar., Granada, Spain.

Grassi, D., N. I. Ignatiev, L. V. Zasova, A. Maturilli, V. Formisano, G. A. Bianchini, and M. Giuranna (2005), Methods for the analysis of data from the Planetary Fourier Spectrometer on the Mars Express mission, *Planet. Space Sci.*, *53*, 1017–1034, doi:10.1016/j.pss.2005.01.006.

Grassi, D., P. Drossart, G. Piccioni, N. I. Ignatiev, L. V. Zasova, A. Adriani, M. L. Moriconi, P. G. J. Irwin, A. Negrão, and A. Migliorini (2008), Retrieval of air temperature profiles in the Venusian mesosphere from VIRTIS-M data: Description and validation of algorithms, *J. Geophys. Res.*, *113*, E00B09, doi:10.1029/2008JE003075.

Ignatiev, N. I., D. Grassi, and L. V. Zasova (2005), Planetary Fourier spectrometer data analysis: Fast radiative transfer models, *Planet. Space Sci.*, *53*, 1035–1042, doi:10.1016/j.pss.2004.12.009.

Krasnopolsky, V. A., and V. A. Parshev (1979), Ozone and photochemistry of the Martian lower atmosphere, *Planet. Space Sci.*, *27*, 113–120, doi:10.1016/0032-0633(79)90040-0.

Lebonnois, S., E. Quèmerais, F. Montmessin, F. Lefèvre, S. Perrier, J.-L. Bertaux, and F. Forget (2006), Vertical distribution of ozone on Mars as measured by SPICAM/Mars Express using stellar occultations, *J. Geophys. Res.*, *111*, E09S05, doi:10.1029/2005JE002643.

Lellouch, E., T. Encrenaz, T. de Graauw, S. Erard, P. Morris, J. Crovisier, H. Feuchtgruber, T. Girard, and M. Burgdorf (2000), The 2.4–45 μm spectrum of Mars observed with the infrared space observatory, *Planet. Space Sci.*, *48*, 1393–1405, doi:10.1016/S0032-0633(00)00118-5.

Lewis, S. R., M. Collins, P. L. Read, F. Forget, F. Hourdin, R. Fournier, C. Hourdin, O. Talagrand, and J.-P. Huot (1999), A climate database for Mars, *J. Geophys. Res.*, *104*(E10), 24,177–24,194, doi:10.1029/1999JE001024.

Lòpez-Valverde, M. A., M. Lòpez-Puertas, J. J. Lòpez-Moreno, V. Formisano, D. Grassi, A. Maturilli, E. Lellouch, and P. Drossart (2005), Analysis of CO2 non-LTE emissions at 4.3 μm in the Martian atmosphere as observed by PFS/Mars Express and SWS/ISO, *Planet. Space Sci.*, *53*, 1079–1087, doi:10.1016/j.pss.2005.03.007.

Montmessin, F., et al. (2006), Subvisible CO2 ice clouds detected in the mesosphere of Mars, *Icarus*, *183*, 403–410, doi:10.1016/j.icarus.2006.03.015.

Montmessin, F., B. Gondet, J.-P. Bibring, Y. Langevin, P. Drossart, F. Forget, and T. Fouchet (2007), Hyperspectral imaging of convective CO2 ice clouds in the equatorial mesosphere of Mars, *J. Geophys. Res.*, *112*, E11S90, doi:10.1029/2007JE002944.

Noe Dobrea, E. Z., J. F. Bell III, M. J. Wolff, and K. D. Gordon (2003), H2O- and OH-bearing minerals in the Martian regolith: Analysis of 1997 observations from HST/NICMOS, *Icarus*, *166*, 1–20, doi:10.1016/S0019-1035(03)00208-2.

Noe Dobrea, E. Z., J. F. Bell III, M. J. Wolff, K. Noll, A. Lubenow, and C. C. Million (2008), Global-scale near infrared variability on Mars: Analysis of 2003 Mars opposition observations from HST/NICMOS, *Icarus*, *193*, 112–124, doi:10.1016/j.icarus.2007.07.026.

Ockert-Bell, M. E., J. F. Bell, J. B. Pollack, C. P. McKay, and F. Forget (1997), Absorption and scattering properties of the Martian dust in the solar wavelengths, *J. Geophys. Res.*, *102*(E4), 9039–9050, doi:10.1029/96JE03991.

Porco, C. C., et al. (2003), Cassini imaging of Jupiter's atmosphere, satellites, and rings, *Science*, *299*, 1541–1547, doi:10.1126/science.1079462.

Rodgers, C. D. (2000), *Inverse Methods for Atmospheric Sounding: Theory and Practice*, World Sci., Singapore.

Schulz, R., J. A. Stuwe, and H. Boehnhardt (2004), Rosetta target comet 67P/Churyumov-Gerasimenko. Postperihelion gas and dust production rates, *Astron. Astrophys., Ser. L*, *422*, 19–21, doi:10.1051/0004-6361:20040190.

Smith, M. D. (2004), Interannual variability in TES atmospheric observations of Mars during 1999–2003, *Icarus*, *167*, 148–165, doi:10.1016/j.icarus.2003.09.010.

Smith, M. D., M. J. Wolff, N. Spanovich, A. Ghosh, D. Banfield, P. R. Christensen, G. A. Landis, and S. W. Squyres (2006), One Martian year of atmospheric observations using MER Mini-TES, *J. Geophys. Res.*, *111*, E12S13, doi:10.1029/2006JE002770.

Spiga, A., F. Forget, B. Dolla, S. Vinatier, R. Melchiorri, P. Drossart, A. Gendrin, J.-P. Bibring, Y. Langevin, and B. Gondet (2007), Remote sensing of surface pressure on Mars with the Mars Express/OMEGA spectrometer: 2. Meteorological maps, *J. Geophys. Res.*, *112*, E08S16, doi:10.1029/2006JE002870.

Wilson, R. J., S. R. Lewis, L. Montabone, and M. D. Smith (2008), Influence of water ice clouds on Martian tropical atmospheric temperatures, *Geophys. Res. Lett.*, *35*, L07202, doi:10.1029/2007GL032405.

Wolff, M. J., and R. T. Clancy (2003), Constraints on the size of Martian aerosols from Thermal Emission Spectrometer observations, *J. Geophys. Res.*, *108*(9), 5097, doi:10.1029/2003JE002057.

E. Ammannito, G. Bellucci, A. Coradini, V. Formisano, D. Grassi, G. Rinaldi, F. Tosi, and P. Wolkenberg, INAF, IFSI, Area della Ricerca di Roma 2 Tor Vergata, Via del Fosso del Cavaliere, I-00133 Rome, Italy. (davide.grassi@ifsi-roma.inaf.it)

G. Arnold, U. Carsenty, R. Jaumann, E. Kuehrt, S. Mottola, G. Neukum, and H. Rauer, DLR, Rutherfordstraße 2, D-12489 Berlin, Germany.

M. A. Barucci, D. Bockelee-Morvan, M. Combes, J. Crovisier, P. Drossart, T. Encrenaz, S. Erard, and D. Tiphene, Observatoire de Paris, Section de Meudon 5, place Jules Janssen, F-92195 Meudon CEDEX, France.

J. Benkhoff, European Space Research and Technology Centre, European Space Agency, Keplerlaan 1, NL-2201 AZ Noordwijk, Netherlands.

J. P. Bibring and Y. Langevin, IAS, Centre universitaire d'Orsay, Bât 120–121, F-91405 Orsay CEDEX, France.

A. Blanco, S. Fonti, and V. Orofino, Dipartimento di Fisica, Università del Salento, Via Arnesano, I-73100 Lecce, Italy.

F. Capaccioni, M. T. Capria, P. Cerroni, M. C. De Sanctis, G. Filacchione, G. Magni, and G. Piccioni, INAF, IASF, Area della Ricerca di Roma 2 Tor Vergata, Via del Fosso del Cavaliere, I-00133 Rome, Italy.

R. Carlson, Jet Propulsion Laboratory, NASA 4800 Oak Grove Drive, Pasadena, CA 91109, USA.

L. Colangeli and V. Mennella, Oss. Astronomico di Capodimonte, INAF, Salita Moiariello, 16, I-80131 Naples, Italy.

M. Combi, Atmospheric, Oceanic, and Space Sciences, University of Michigan, Space Research Building, 2455 Hayward Street, Ann Arbor, MI 48109-2143, USA.

C. Federico, Dipartimento di Scienze della Terra, Università di Perugia, Piazza Università, I-06123 Perugia, Italy.

U. Fink, Department of Planetary Sciences, Lunar and Planetary Laboratory, 1629 East University Blvd., Tucson, AZ 85721, USA.

W.-H. Ip, Graduate Institute of Astronomy, National Central University, 300 Chung-Da Road TW, Chung-Li 32054, Taiwan.

P. G. J. Irwin and F. W. Taylor, Atmospheric, Oceanic and Planetary Physics, University of Oxford, Clarendon Laboratory Parks Road, Oxford OX1 3PU, UK.

T. McCord, Bear Fight Center, PO Box 667, Winthrop, WA 98862, USA.

P. Palumbo, Dipartimento di Scienze Applicate–Università degli Studi di Napoli "Parthenope," Via De Gasperi 5, I-80133 Naples, Italy.

B. Schmitt, OSUG, Université Joseph Fourier, Bâtiment D de Physique, 122 rue de la Piscine, BP 53, F-38041 Grenoble CEDEX 9, France.

G. P. Tozzi, Oss. Astrofisico di Arcetri, INAF, Largo Enrico Fermi 5, I-50125 Firenze, Italy.